Effects of Porous Gap Fillers on Leading-Edge Slat Noise of 30P30N. Part II: PIV Measurements

Yang Zhang* and Louis N. Cattafesta III[†]

Florida Center for Advanced Aero-Propulsion (FCAAP), Florida A&M University and Florida State University, Tallahassee, Florida, 32310, US

Meelan M. Choudhari,[‡] Kyle A. Pascioni,[§] Mehdi R. Khorrami,[¶] David P. Lockard,[‖] and Travis Turner[**]

NASA Langley Research Center, Hampton, VA, 23681, US

The leading edge slat of a high-lift system is one of the main contributors to the airframe noise during approach conditions. This paper, the second of two parts, continues our previous studies on the slat gap filler as a passive noise control device on the two-dimensional, 30P30N multielement airfoil. Whereas the earlier study was focused on the effects of an impermeable gap filler that completely blocks the flow through the gap, this follow-on assessment is devoted to permeable slat gap fillers that allow limited amounts of flow to pass through the gap. Part I of this two-part investigation described the aerodynamic and acoustic effects of the permeable gap fillers, as inferred from both the measurements of static and unsteady surface pressures and the microphone array data for the radiated noise. To understand the physical mechanism responsible for the noise reduction documented in Part I, as well as for the accompanying aerodynamic penalty due to the porous gap fillers, Particle Image Velocimetry (PIV) is used in this paper to measure the flow details in the slat-cove region of the 30P30N model. A single angle of attack ($\alpha = 5.5°$) and a chord-based Reynolds number of 1.71×10^6 are selected as the test conditions. The PIV results show that the slat flow features are significantly altered with the presence of the porous gap filler, resulting in a more stable slat-cove shear layer and, thus, reduced velocity fluctuations with a successive decrease in the permeability. The porous gap filler with the lowest permeability acts similar to the solid gap filler. However, flow separation is observed on the upper side of the porous interface, which leads to an aerodynamic performance penalty via a reduction in lift on the main wing.

Nomenclature

c	=	stowed chord, [m]
d	=	slice-cut distance, [m]
l	=	slat extension length, [m]
S	=	shear layer trajectory length, [m]
S_b	=	shear layer trajectory length for baseline, [m]
St	=	Strouhal number
s	=	slat chord, [m]
U_∞	=	freestream velocity, [m/s]
u	=	velocity in the streamwise direction, [m/s]
v	=	velocity in the normal direction, [m/s]
x	=	chordwise direction, [m]
y	=	normal direction, [m]

*Research Faculty, Department of Mechanical Engineering, AIAA Member. yz12b@fsu.edu

[†]Professor and University Eminent Scholar, Department of Mechanical Engineering, AIAA Associate Fellow.

[‡]Aerospace Technologist, Computational AeroSciences Branch, AIAA Fellow.

[§]Research Aerospace Engineer, AIAA Member.

[¶]Aerospace Technologist, Computational AeroSciences Branch, AIAA Associate Fellow.

[‖]Aerospace Technologist, Computational AeroSciences Branch, AIAA Associate Fellow.

[**]Aerospace Technologist, Computational AeroSciences Branch, AIAA Associate Fellow.

α = angle of attack, [°]
δ_ω = vorticity thickness, [m]
ω = spanwise vorticity, [1/s]

I. Introduction

In our past studies [1–4], we evaluated the noise control performance of several passive treatments and applied Particle Image Velocimetry (PIV) to elucidate the noise suppression mechanisms. Among the different treatments, both slat cove filler and gap filler were able to suppress the narrowband peaks associated with the slat-cove shear layer and broadband noise components. However, the physical mechanisms of these two treatments are different. The slat cove filler totally eliminates the flow separation at the slat cusp, while the gap filler alters the slat-cove shear layer impingement to farther downstream on the main wing leading edge. Although aerodynamic penalty (i.e., loss of lift) was observed in our previous study, a similar concept did not show this drawback in other studies [5, 6]. This indicates the gap filler geometry profile needs to be more streamlined to reduce/eliminate the flow separation. As an alternate means of flow and noise control, the permeability of the gap filler interface could be tuned to allow a portion of the flow to pass through the gap between the slat and the main wing instead of a total blockage. In Part I, we presented the steady/unsteady surface pressures and far-field acoustics of 30P30N with porous gap filler installed as a noise control device. Similar to the rigid gap filler [2], all porous gap fillers were able to suppress the narrowband peaks of far-field acoustic spectra. The porous gap fillers with medium and lowest permeability were found to also reduce the broadband component of noise by approximately 10 dB. Although noise reduction is achieved via applying the porous gap fillers, they all exhibit aerodynamic penalties. The pressure coefficient increases in magnitude near the main wing leading edge on the suction side, which is similar to the solid gap filler. However, the loss of aerodynamic lift in comparison with the nonporous gap filler indicates that flow separation may occur above the porous gap fillers, similar to the observations for the solid gap filler [3]. In order to visualize the flow field in the slat region with the porous gap filler installed, PIV is used to measure the flow field in the vicinity of the gap fillers. In part II, we focus on describing of the PIV investigations of the porous gap fillers.

II. Experimental setup

As described in further detail in Part I, the current study was carried out in the Florida State Aeroacoustic Tunnel (FSAT) facility located at the Florida Center for Advanced Aero-Propulsion (FCAAP) at the Florida State University (FSU). The wind tunnel Kevlar panels are replaced with glass panels for the optical access. The test section dimensions in the streamwise, spanwise, and vertical directions correspond to L=2.74 m, W=1.22 m, and H=0.91 m, respectively. The schematic of the two-dimensional airfoil model are provided in Figure 1. The coordinate system indicated in red is used for PIV plots with its origin at the leading edge of the stowed airfoil, in which x represents the streamwise direction, y is normal to the airfoil chord line, and z is along the airfoil span to make a right-handed system.
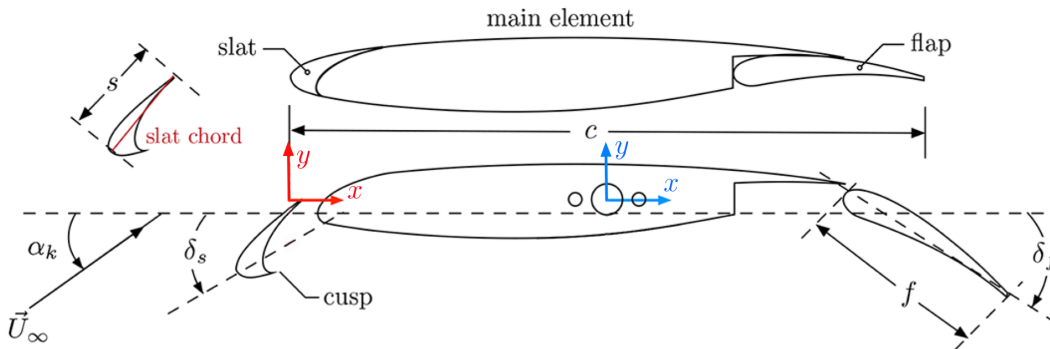

Fig. 1 Schematic of the 30P30N multielement airfoil.

A. Porous gap fillers

Details of the porous samples and installations are given in Part I. However, to keep the discussion self-contained, a picture of the samples is shown in Figure 2. The permeability reduces from sample H to L, with the flow resistance of the samples being $0.08\rho_0 c_0$, $0.24\rho_0 c_0$, and $0.72\rho_0 c_0$, respectively. Sample H is soft similar to a fabric, while sample L has the most stiffness.
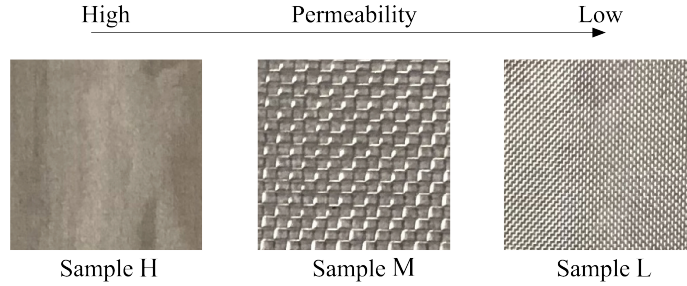

High   Permeability   Low

Sample H   Sample M   Sample L

Fig. 2   Pictures of three porous samples.

(a) Installation of sample H   **(b) Installation of sample M or L**   **(c) Picture of installed sample H**
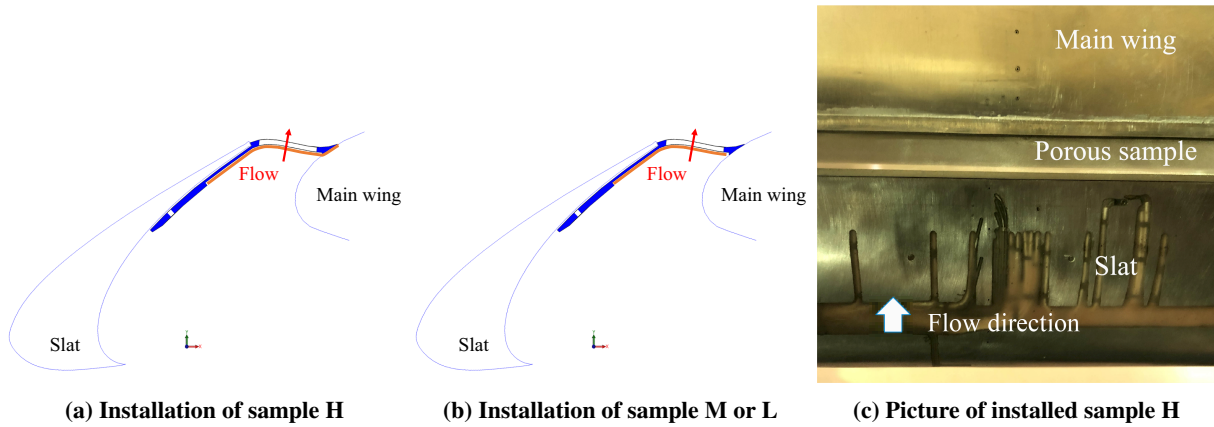
Fig. 3   Installation of porous samples.

B. Particle Image Velocimetry setup

A schematic of the PIV setup is provided in Figure 4a. The 30P30N model has a geometric angle of attack of 5.5°, which is aerodynamically equivalent to the baseline case of 8° in the Kevlar wall test section [7]. Due to the complicated geometry of the multielement airfoil, shadow regions would appear if the model was only illuminated on one side. Therefore, the laser beam from an Evergreen 400 mJ Nd:YAG laser is split by a combination of 532 nm coated beam expander and a coated plate beam splitter. Each laser beam passes through different combinations of optics and forms a laser sheet to simultaneously illuminate the pressure and suction sides of the slat region at the midplane of the model. The laser sheet illuminates the cove region from the upstream side such that a portion of the flow field is in the shadow region. Two Imager sCMOS cameras (2560 × 2160 pixels) are secured underneath the acrylic side wall with the optical axes orthogonal to the laser sheets (Figure 4b). To capture the small field of view, the two cameras are equipped with different combinations of lenses and are located at different distances from the laser sheets. This allowed for a small overlap region required to stitch the vector fields together. The camera looking at the pressure side of the slat region is equipped with a SIGMA 105 mm f/2.8 macro lens with a 1.4× teleconverter, while the other one is equipped with a TAMRON 180 mm f/3.5 macro lens with a 27.5 mm spacer. Two 532 nm bandpass filters are used to remove ambient light. Fluorescent orange tape (3M) is applied on the model surface to reduce the laser reflections. Calibration is performed prior to the data acquisition with a LaVision type-22 calibration plate. Olive oil is used in a TSI 9307-6 seeder to generate the tracer particles, which are injected into the flow at the downstream of the inlet screen. The double-frame image pairs are acquired at a sampling rate of 10 Hz with a nominal number of 550 vector fields

obtained for each case using LaVision DaVis 8.4.0 software.

The data are processed by using the same software as that used for the data acquisition. For each data set, the background noise is first subtracted from the images to enhance the signal-to-noise ratio. Geometric and algorithmic masks are applied within the measurement domain to cover the model geometry and any regions of low seeding density. Then, a multipass cross-correlation scheme using a window size from 256×256 pixels to 32×32 pixels is used to obtain the particle displacements between image pairs. Universal outlier detection [8] is applied to remove the spurious vectors, and then the resulting two vector fields from each camera are merged. The stitched vector field is finally post-processed using multivariate outlier detection [9] in MATLAB. The resulting vector resolution is approximately 5.4 vectors/mm.
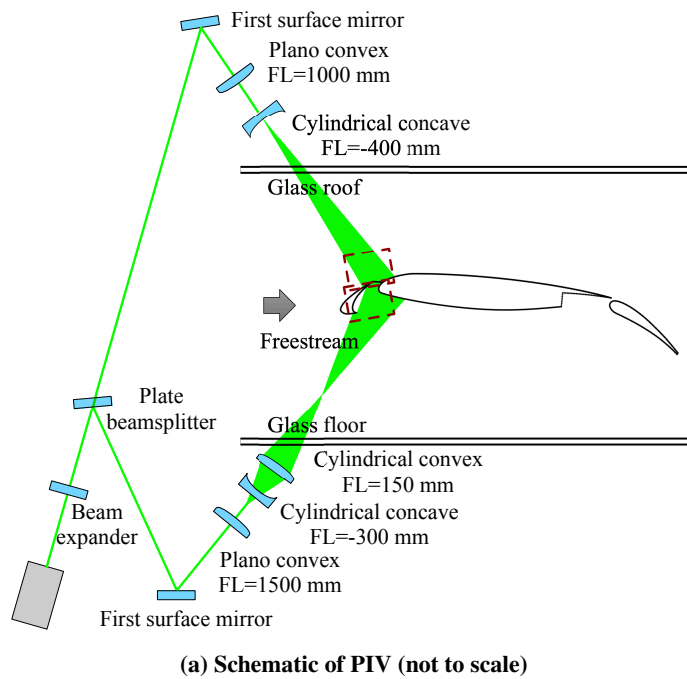

(a) Schematic of PIV (not to scale)

(b) PIV cameras

Fig. 4   PIV experiment setup.

III. Results and discussion

A. Porous gap fillers

Note that the results of the baseline case in the current paper are from our previous study [3]. The ensemble averaged $u-$ and v-velocity components are represented via streamlines and quiver vectors, respectively, shown in Figures 5 and 6 for the three porous gap filler cases. The blank region inside the slat cove is due to the blockage of the laser sheet, and a small region on either side of the porous opening is masked out due to strong reflections. The slat-cove shear layer trajectories are changed for all three porous gap filler cases. Similar to the previous solid gap filler case [2], the slat-cove shear layer does not reattach to the slat cove surface, but it reattaches to the main wing leading edge. The altered shear layer trajectory is associated with a large recirculation bubble in the cove region. The size of the recirculation bubble is inversely proportional to the permeability. As the permeability increases, more flow passes through the gap such that the circulation bubble is pulled toward the gap resulting in a reduced extent (compare Figure 5b with Figure 5d). The second significant change is the wake region on the upper side of the porous gap filler. In the baseline case, the flow accelerates when passing through the gap. However, the flow speed is much lower when passing through the porous media, resulting in a large velocity gradient normal to the main wing surface. Although sample L has the minimal permeability among the three gap filler designs and the flow feature is similar to the solid gap filler, the mechanism for the flow separation on the upper side of the gap filler is different. The flow separates at the slat to gap filler junction in the rigid gap filler case, while the flow separates at the gap filler and main wing junction in the sample L case. With the

4

increased permeability, more low speed flow enters the upper high speed flow region through the porous medium.

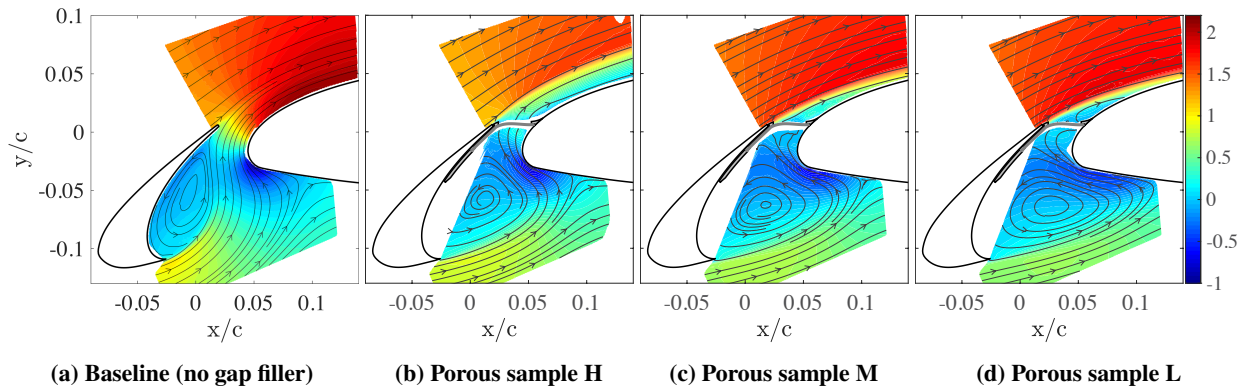| (a) Baseline (no gap filler) | (b) Porous sample H | (c) Porous sample M | (d) Porous sample L |

Fig. 5   Ensemble averaged u-component of baseline case vs. porous gap filler cases (from high permeability to low permeability) with streamlines at $\alpha = 5.5°$.

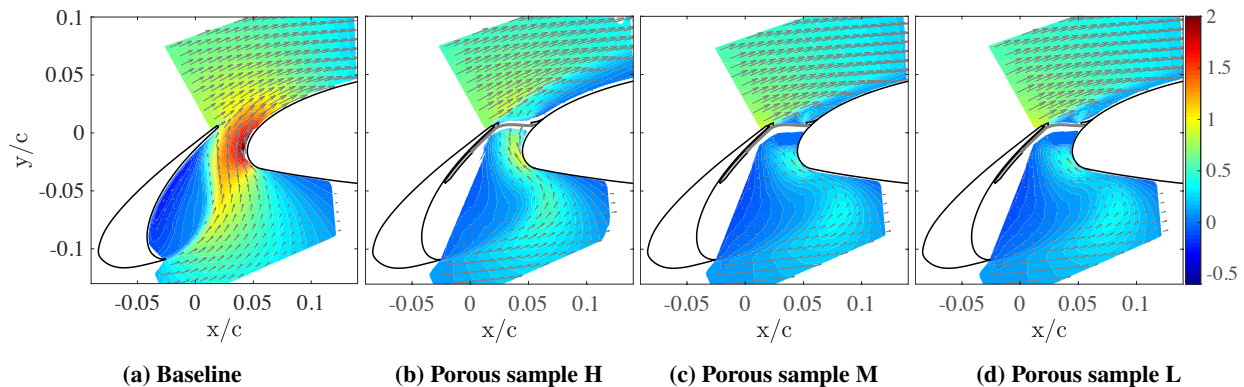| (a) Baseline | (b) Porous sample H | (c) Porous sample M | (d) Porous sample L |

Fig. 6   Ensemble averaged v-component of baseline case vs. porous gap filler cases (from high permeability to low permeability) with vectors at $\alpha = 5.5°$.

The ensemble-averaged spanwise vorticity $\omega_z c / U_\infty$ for all four cases is compared in Figure 7. The shear layer and wake regions can be identified as the regions of high vorticity magnitude, i.e., positive vorticity (red) for the slat-cove shear layer and negative vorticity (blue) for the slat trailing edge shear layer. The slat-cove shear layer in the baseline (no-gap-filler) case has the highest level of positive vorticity, and the vorticity level decreases with the decrease of the permeability. The trajectory of the slat-cove shear layer tends to become more straight from porous sample H to sample L. The trend implies that the trajectory of the slat-cove shear layer can be tuned via the permeability of the porous sample. It is clear that, relative to the baseline case, the vorticity distribution is more diffuse for the highest porosity gap filler (sample H) and even more so for the gap fillers with successively lower permeability. Regardless of the aerodynamic performance, the manipulation of the slat-cove shear layer can lead to a diffuse shear layer impinging less intensely at a different location along the airfoil surface. This should weaken the acoustic feedback mechanism or even totally disrupt the fluid-acoustic feedback similar to the solid gap filler case [2]. The negative vorticity in the slat trailing edge shear layer has the inverse trend compared to the vorticity in the slat-cove shear layer. The negative vorticity increases in magnitude with the decrease of the permeability. This is due to the successively slower flow entering the upper side of the gap filler with a lower permeability. With less amount of flow entering the suction side of the main wing, the trajectory of the slat trailing edge shear layer bends toward the main wing leading edge.

The turbulent kinetic energy (TKE) levels for the different porous sample cases (as shown in Figures 8a to 8d) clearly show that the velocity fluctuations in the slat-cove shear layer are significantly reduced. Unlike the observations of vorticity, the trend of TKE with the permeability is quite different. The TKE level in the shear layer attains its maximum around $x/c = 0.04$ and then decays in the sample H case. From the measured PIV domain, the TKE level in this case is comparable to the baseline case. With the decrease of permeability, the TKE level is reduced to lower than the baseline
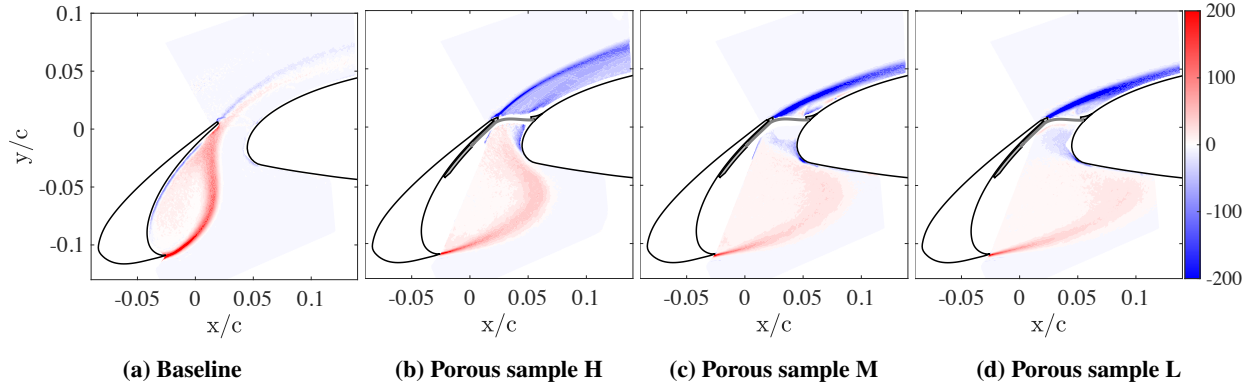
(a) Baseline   **(b) Porous sample H**   **(c) Porous sample M**   **(d) Porous sample L**

Fig. 7   Averaged spanwise vorticity $\omega_z c / U_\infty$ of baseline case vs. porous gap filler cases at $\alpha = 5.5°$.

case. High levels of TKE are also observed just upstream of the porous opening inside the cove in the sample H case. At the upper side of the porous gap filler, it is noted that the porous sample H reduces the TKE level near the slat trailing edge. It is also observed that the TKE in the wake introduced by the gap filler junction on the main wing is comparable to the slat trailing edge shear layer. With the decrease of the permeability, the TKE level near the slat trailing edge becomes higher, and the high TKE region gets closer to the main wing surface. The wake region induced by the gap filler junction on the main wing is suppressed in extent. Even though there is only a small amount of flow through the porous opening in sample L, the TKE level is significantly less than the solid gap filler case.
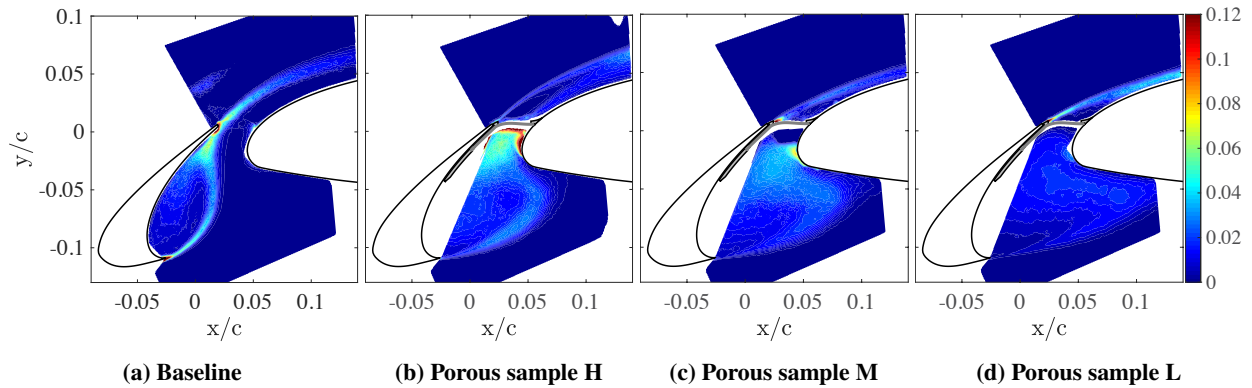

(a) Baseline   **(b) Porous sample H**   **(c) Porous sample M**   **(d) Porous sample L**

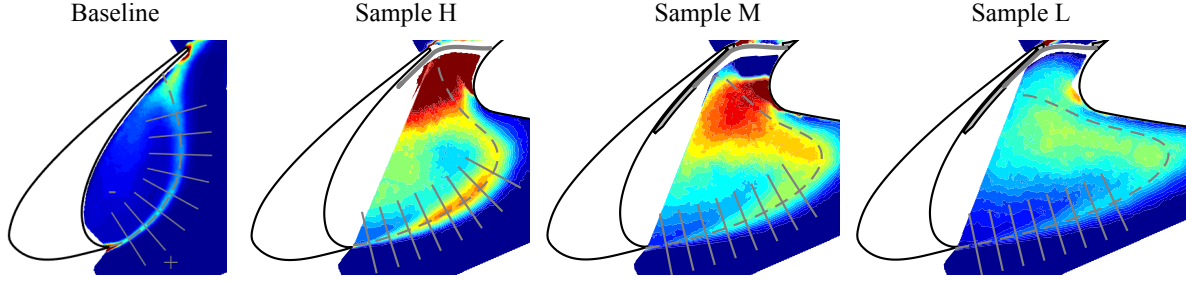**Fig. 8   TKE of baseline case vs. porous gap filler cases at $\alpha = 5.5°$.**

Fig. 9   Slice-cuts normal to the dividing streamline in the porous gap filler cases. Note that the contour levels are adjusted differently to highlight the high TKE in the shear layer.

The flow properties of different cases are compared at several stations along the trajectory of the slat-cove shear layer. The dashed lines depicted in Figure 9 represent the streamline along the slat-cove shear layer. Note that the spacing between each slice-cuts equals $0.1S_b$, where S_b is the arclength of the shear layer in the baseline case. The slice-cuts are normalized by the chord length c, extending from $-0.02c$ to $0.02c$ with the profile distance d increasing outward from the recirculation bubble. The flow data along each slice-cut are interpolated, extracted, and compared in Figure 10. From Figure 10a, it is clear that the TKE level in the porous sample cases are initially lower than those in the baseline case. The sample H case is approximately 50% of the baseline case while the other porous cases are even lower. As the shear layer develops, the peak TKE levels in the sample H and sample M cases grow to a higher level than the baseline case starting at $S/S_b = 0.3$ and 0.5 locations, respectively. For the lowest permeability case, i.e., sample L, the peak TKE level is always lower than the baseline case, similar to the rigid gap filler case. The TKE levels in the freestream ($d/c = 0.02$) are comparable in different cases as expected. However, the TKE levels in the recirculation region are generally higher in the porous sample cases than the baseline case, indicating that the recirculation bubble is more unsteady with the porous gap filler installed, especially with sample H. Of course, we note the frequency spectrum of the unsteady fluctuations is also an important consideration from the standpoint of radiated noise. The current non-time-resolved PIV data does not provide that information. However, we note that the dominant frequencies associated with the shear layer unsteadiness are associated with the frequencies of most amplified shear layer instabilities and those, in turn, can be related to shear layer characteristics such as the vorticity thickness, velocity ratio, etc. [10]. The variation in shear layer thickness along the shear layer trajectory is considered later in this section. At each trajectory location, the peak shear layer vorticity in the porous gap filler cases is lower than that in the baseline, i.e., no gap filler case. The sample H case has slightly higher peak vorticity levels than the other two samples with lower permeabilities. The vorticity profiles of samples M and L are collapsed at all locations. Again, the velocity components are projected to a local coordinate defined by the slice-cuts. Then the local vorticity thickness is calculated as $U_{\text{edge}}/(\partial u/\partial d)_{\text{max}}$, where U_{edge} is the velocity at $d/c = 0.02$. The vorticity thickness across the different cases is compared in Figure 11. The porous sample cases clearly have a larger spreading rate than the baseline case with a comparable value of the initial vorticity thickness. Among the porous gap filler cases, samples M and L have comparable spreading rates that are higher than that in the sample H case, and the faster spreading of the shear layer results in a lower TKE level as shown in Figures 8c and 8d.

Analogous profiles are also extracted from a series of cuts (Table 1) in the slat trailing edge wake, which are labeled as $w_1, w_2, \ldots, w_{10}$ in Figure 12. From the comparison of the extracted profiles shown in Figure 13, it is clear that both TKE and vorticity exhibit quite different trends in the porous gap filler cases than the baseline case. In Figure 13a, the TKE profiles in the sample H case and the baseline case, respectively, have comparable peak levels. As the permeability decreases, the peak TKE levels at location w_1 for the sample M and L cases are significantly higher than that in sample H case, indicating more unsteadiness in slat trailing edge shear layer. This is due to the increasingly lower speed flow passing through the porous media as the permeability decreases. One distinguishing behavior of the profiles in the sample H case is the presence of the double peaks starting at the w_5 location. Note that the positive d/c is toward the main wing surface, the peak in the negative d/c is attributed to the shear layer from the slat trailing junction, while the peak in the positive positive d/c is due to the junction between the gap filler and main wing. The amount of flow entering the upper side of the porous gap filler governs the shear layer trajectory from the slat trailing edge. In the sample M and sample L cases, with less flow entering the upper side, the TKE peak moves in the positive d/c direction, and only one peak is observed. This indicates the shear layer gets closer to the main wing surface. The least permeable sample L shows the largest TKE level at all locations.
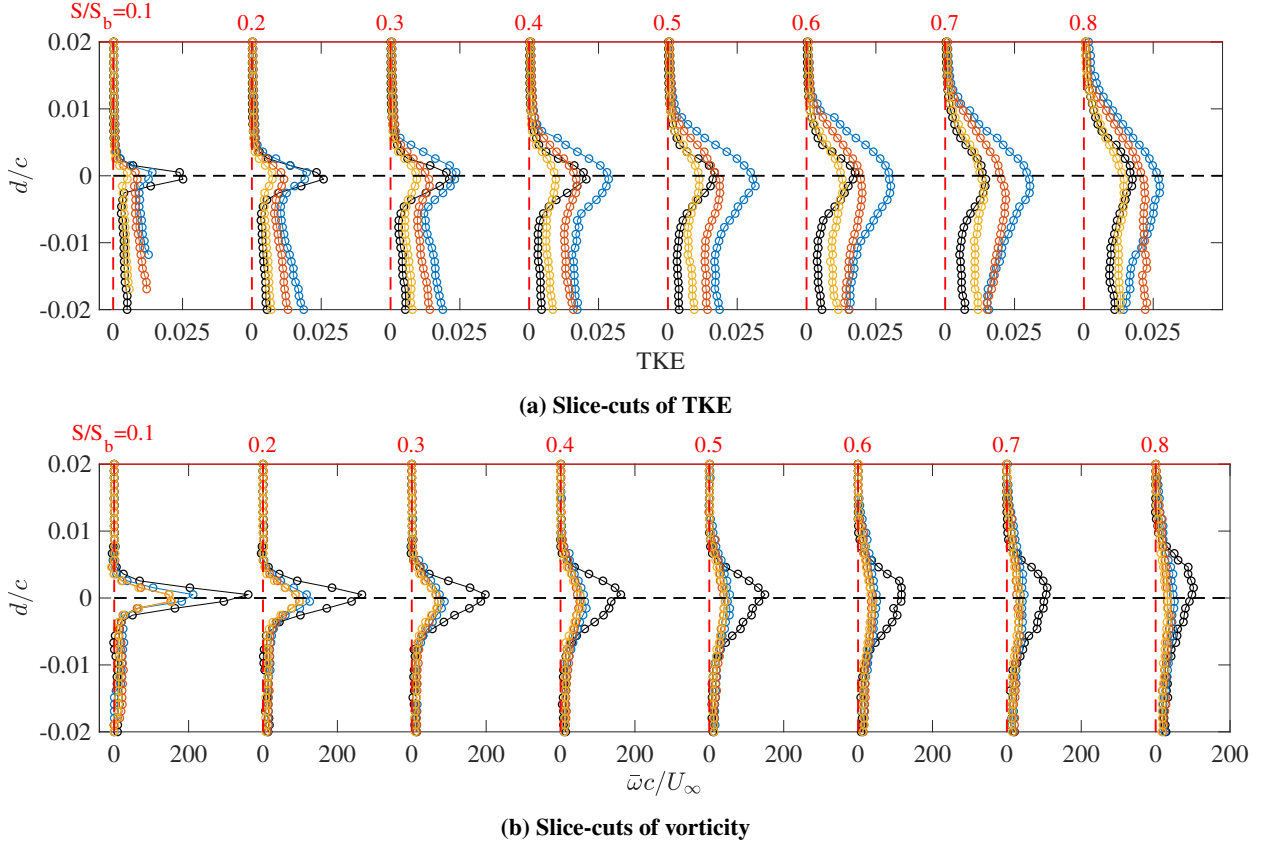
(a) Slice-cuts of TKE

(b) Slice-cuts of vorticity

Fig. 10 **Slice-cuts of TKE and vorticity using S/S_b scaling in the slat-cove shear layer. ○: baseline; ○: Sample H; ○: Sample M; and ○: Sample L.**
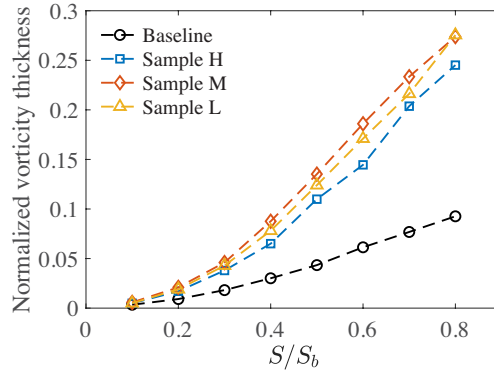

Fig. 11 **Nondimensional vorticity thickness for baseline and porous gap filler cases.**

Table 1 **Slices of slat trailing edge shear layer for baseline and porous gap filler cases. Distance is normalized by c ($\times 10^{-3}$).**

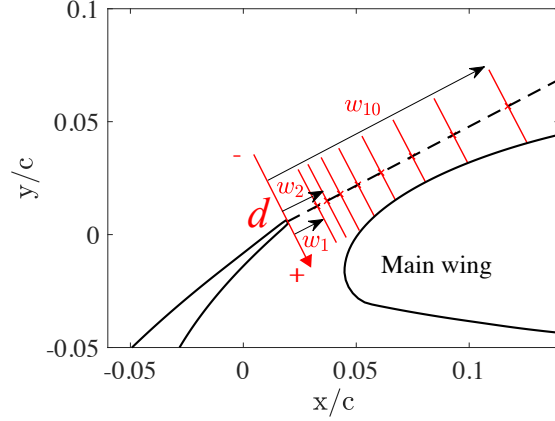| w_1	w_2	w_3	w_4	w_5	w_6	w_7	w_8	w_9	w_{10}
6.855	9.094	7.541	16.132	21.433	28.517	37.885	50.407	66.996	89.115

Fig. 12 Slices of slat trailing edge shear layer for baseline and porous gap filler cases.

The vorticity profiles at w_1 show comparable peak levels for all three porous samples, and those levels are significantly higher than those in the baseline case. Again, a double-peak vorticity profile is observed in the sample H case, which is due to the two flow separations in the wake as explained previously. The vorticity peak levels become comparable in sample M and L cases at w_7 location and thereafter. Note that the current gap filler skeleton is not ideal as the junction on the main wing caused the flow separations near the main wing. The effects of the gap filler skeleton without porous skin are evaluated in the following section.
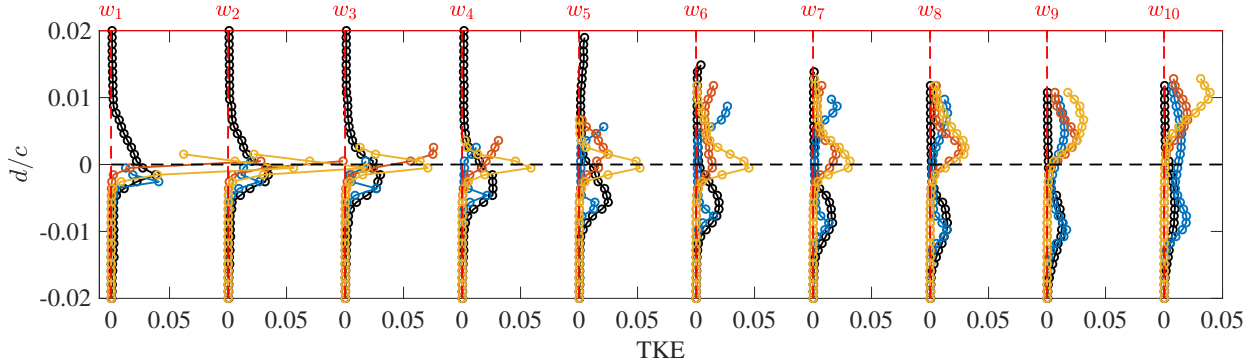
(a) Slice-cuts of TKE
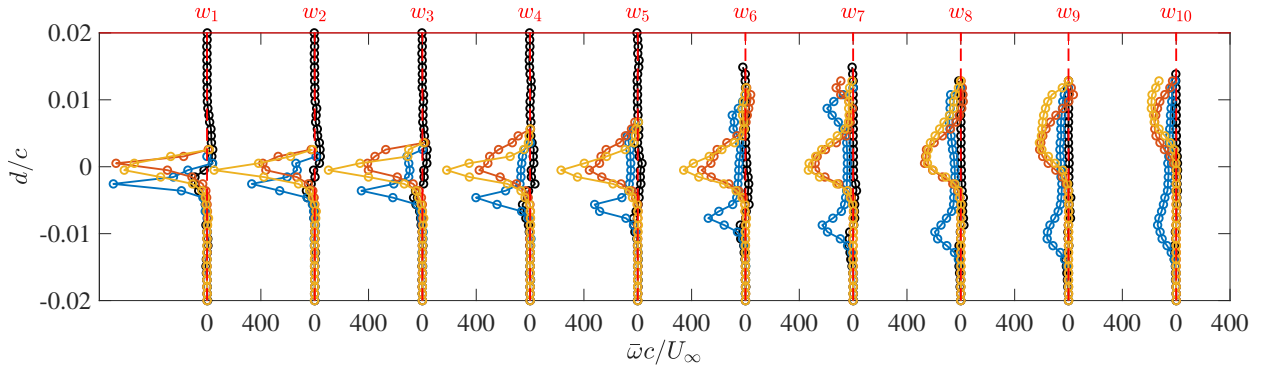
(b) Slice-cuts of vorticity

Fig. 13 Slice-cuts of TKE and vorticity using S/S_b scaling in the slat trailing edge wake. ∘: baseline; ∘: Sample H; ∘: Sample M; and ∘: Sample L.

9

B. Gap filler skeleton

An additional case, the gap filler skeleton without the porous skin, was studied to understand the effects of the add-on structure besides the porous media on the flow field. The gap filler skeleton and the baseline cases are compared in Figure 14. Theoretically, the skeleton should allow the flow to pass through the gap similar to that in the baseline case, with the exception of minor additional blockage to the structure. However, the junction on the main wing leading edge causes flow separation and introduces a long recirculation bubble on the main wing surface. The presence of the junction also slows down the local flow passing through the gap considering the lower level of $v-$component at the gap in Figure 14d. In the porous gap filler cases, an enlarged recirculation bubble in the slat cove is associated with a slower flow through the gap. Similar flow features are observed in the skeleton case in that the shear layer path is elongated (more curved) relative to the baseline case, and the recirculation bubble size is increased. The most significant drawback of the skeleton is the flow separation on the main wing that results in the pressure increase on the suction side of the main wing, i.e., a severe aerodynamic penalty.
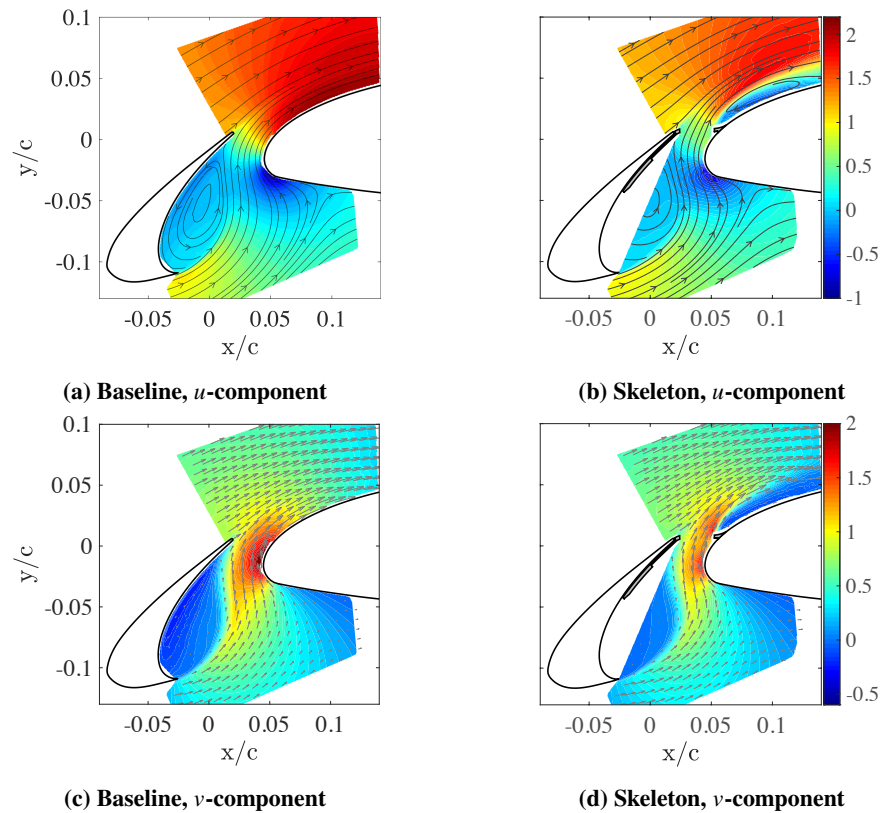

(a) Baseline, *u*-component

(b) Skeleton, *u*-component

(c) Baseline, *v*-component

(d) Skeleton, *v*-component

Fig. 14   Ensemble averaged *u* and *v*-component of baseline case vs. gap filler skeleton case with streamlines and quiver vectors overlaid, respectively, at $\alpha = 5.5°$.

IV. Conclusions

The current research has extended our previous study [1] on passive control devices to reduce the slat noise from a high-lift airfoil system. Specifically, as an extension to the previously studied solid gap filler concept, we investigated three porous gap fillers that allow increasing amounts of flow to pass through the slat gap. The PIV technique was used to measure the flow field in the slat region by illuminating the model from both sides of the gap filler. The resistivity of the porous medium regulates the amount of the flow across the gap filler, resulting in different trajectories and other significant characteristics of the slat-cove shear layer for the three gap filler designs examined herein. For the gap filler with the lowest permeability, the slat-cove shear layer is similar to the one for the solid gap filler. In general, a higher blockage imposed at the gap leads to a larger size of the recirculation bubble within the cove and a more diffuse and, hence, more stable slat cover shear layer. The flow-acoustic feedback loop is thus altered or even eliminated with the

presence of a gap filler, with each design resulting in the suppression of the narrowband peaks in the acoustic spectra as measured for the baseline case with no gap filler. The PIV data also shed useful light on the adverse aerodynamic effects of the porous gap fillers used in this particular experiment. The gap filler junction is shown to induce a large wake region for the gap filler design with the highest permeability, but the wake becomes less significant with a decreasing permeability as the shear layer from the slat trailing edge shifts progressively closer to the main wing surface. In general, the wake and the shear layer result in an increased pressure on the suction side of the main wing, resulting in the observed loss in lift. By examining the case with just the skeleton that otherwise holds the porous gap filler, we observed a large flow separation caused by the skeleton junction with the main wing. Any such obstacles on the main wing should, therefore, be avoided in future designs.

Acknowledgement

References

[1] Zhang, Y., ONeill, A., Cattafesta, L. N., Pascioni, K., Choudhari, M., Khorrami, M. R., Lockard, D. P., and Turner, T., "Assessment of Noise Reduction Concepts for Leading-Edge Slat Noise," *2018 AIAA/CEAS Aeroacoustics Conference*, American Institute of Aeronautics and Astronautics, 2018. https://doi.org/10.2514/6.2018-3461, AIAA Paper 2018-3461.

[2] Zhang, Y., Cattafesta, L. N., Pascioni, K. A., Choudhari, M. M., Lockard, D. P., Khorrami, M. R., and Turner, T., "Slat Noise Control Using a Slat Gap Filler," *AIAA AVIATION 2020 FORUM*, 2020. https://doi.org/10.2514/6.2020-2553, AIAA paper 2020-2553.

[3] Zhang, Y., Richardson, R., Cattafesta, L. N., Choudhari, M. M., Pascioni, K. A., Khorrami, M. R., Lockard, D. P., and Turner, T. L., "Investigation of the 30P30N Slat Flow Field with Passive Control Devices Using Particle Image Velocimetry," *AIAA AVIATION 2021 FORUM*, American Institute of Aeronautics and Astronautics, 2021. https://doi.org/10.2514/6.2021-2116, AIAA Paper 2021-2116.

[4] Zhang, Y., Cattafesta, L. N., Pascioni, K. A., Choudhari, M. M., Khorrami, M. R., Lockard, D. P., and Turner, T., "Assessment of Slat Extensions and a Cove Filler for Slat Noise Reduction," *AIAA Journal*, Vol. 59, No. 12, 2021, pp. 4987–5000. https://doi.org/10.2514/1.j060502.

[5] Mu, M. S., Schrass, J., Lieb, K. F., and Hartl, D. J., "Aerodynamic and Aeroacoustic Experimentation of a Slat-Gap Filler for Airframe Noise Reduction," *AIAA Scitech 2021 Forum*, American Institute of Aeronautics and Astronautics, 2021. https://doi.org/10.2514/6.2021-1997, AIAA Paper 2021-1997.

[6] Lockard, D. P., Turner, T. L., Bahr, C. J., and Hutcheson, F. V., "Overview of Aeroacoustic Testing of the High-Lift Common Research Model," *AIAA AVIATION 2021 FORUM*, American Institute of Aeronautics and Astronautics, 2021. https://doi.org/10.2514/6.2021-2113, AIAA Paper 2021-2113.

[7] Pascioni, K., "An Aeroacoustic Characterization of a Multi-Element High-Lift Airfoil," Ph.D. thesis, Florida State University, Tallahassee, FL, 2017.

[8] Westerweel, J., and Scarano, F., "Universal Outlier Detection for PIV Data," *Experiments in Fluids*, Vol. 39, No. 6, 2005, pp. 1096–1100. https://doi.org/10.1007/s00348-005-0016-6.

[9] Griffin, J., Schultz, T., Holman, R., Ukeiley, L. S., and Cattafesta, L. N., "Application of Multivariate Outlier Detection to Fluid Velocity Measurements," *Experiments in Fluids*, Vol. 49, No. 1, 2010, pp. 305–317. https://doi.org/10.1007/s00348-010-0875-3.

[10] Choudhari, M. M., and Khorrami, M. R., "Effect of Three-Dimensional Shear-Layer Structures on Slat Cove Unsteadiness," *AIAA Journal*, Vol. 45, No. 9, 2007, pp. 2174–2186. https://doi.org/10.2514/1.24812.